Observations of grain-boundary phase transformations in an elemental metal

https://doi.org/10.1038/s41586-020-2082-6

Received: 30 September 2019

Accepted: 29 January 2020

Published online: 18 March 2020

Check for updates

Thorsten Meiners[1], Timofey Frolov[2,3]✉, Robert E. Rudd[2], Gerhard Dehm[1,3]✉ & Christian H. Liebscher[1,3]✉

The theory of grain boundary (the interface between crystallites, GB) structure has a long history[1] and the concept of GBs undergoing phase transformations was proposed 50 years ago[2,3]. The underlying assumption was that multiple stable and metastable states exist for different GB orientations[4–6]. The terminology 'complexion' was recently proposed to distinguish between interfacial states that differ in any equilibrium thermodynamic property[7]. Different types of complexion and transitions between complexions have been characterized, mostly in binary or multicomponent systems[8–19]. Simulations have provided insight into the phase behaviour of interfaces and shown that GB transitions can occur in many material systems[20–24]. However, the direct experimental observation and transformation kinetics of GBs in an elemental metal have remained elusive. Here we demonstrate atomic-scale GB phase coexistence and transformations at symmetric and asymmetric [11$\bar{1}$] tilt GBs in elemental copper. Atomic-resolution imaging reveals the coexistence of two different structures at Σ19b GBs (where Σ19 is the density of coincident sites and b is a GB variant), in agreement with evolutionary GB structure search and clustering analysis[21,25,26]. We also use finite-temperature molecular dynamics simulations to explore the coexistence and transformation kinetics of these GB phases. Our results demonstrate how GB phases can be kinetically trapped, enabling atomic-scale room-temperature observations. Our work paves the way for atomic-scale in situ studies of metallic GB phase transformations, which were previously detected only indirectly[9,15,27–29], through their influence on abnormal grain growth, non-Arrhenius-type diffusion or liquid metal embrittlement.

Here we focus on Σ19b [11$\bar{1}$] tilt boundaries obtained by thin-film deposition of copper (Cu) on (0001)-oriented sapphire substrate[30] (see Methods and Extended Data Fig. 1). Figure 1 shows two variants of GB phase transitions imaged at atomic resolution. The phase transition illustrated in Fig. 1a, b occurs at a near-symmetric GB, the one shown in Fig. 1c at a vicinal boundary. Since the grains remain the same across the structure change, the GB has the same misorientation. The two structures are two phases of the same GB. In both cases, two sets of characteristic structural units, referred to as pearl (blue) and domino (red) structures, coexist. The near-symmetric boundary (Fig. 1a) has a measured misorientation angle of about 48° and the GB plane inclination deviates about 1° from the perfect symmetric orientation. A domino structure (red) segment about 11 nm long is embedded between two pearl segments (pearl) and the GB clearly follows a slight curvature leading to local deviations of the GB plane orientation of about 5°. However, facet formation is not observed. The magnified view of the right transition is shown in Fig. 1b. The domino structure is composed of double-square units alternating between low and high inclinations, as also shown in Fig. 1d. The structural unit of the pearl segment is characterized by an alternation of curved and square-type segments (see also Fig. 1e). Both structures are separated by a GB phase junction, that is, a line defect whose line direction is perpendicular to the image plane.

The same GB phase transition is observed for a vicinal [11$\bar{1}$] tilt GB with an inclinational deviation of about 5° as shown in Fig. 1c. The structural units of the domino and pearl structures are nearly identical to the symmetric boundary of Fig. 1a and their detailed atomic arrangement is highlighted in Fig. 1d, e. A closer inspection of the domino structure of Fig. 1d reveals that the double-square units show an alignment and sequence similar to those of the symmetric boundary of Fig. 1a, b. In both cases, the regular order of the domino units is interrupted by irregular or disordered regions. The sequence of base structural units of the pearl structure, curved and square segments, is interrupted by curvy or linear subunits, as shown in Fig. 1b, e. The observations reveal that two GB motifs can coexist at a symmetric and an asymmetric GB without change in GB plane orientation, misorientation and composition, showing all the features of a congruent GB phase transition.

[1]Max-Planck-Institut für Eisenforschung, Düsseldorf, Germany. [2]Lawrence Livermore National Laboratory, Livermore, CA, USA. [3]These authors jointly supervised this work: Timofey Frolov, Gerhard Dehm, Christian H. Liebscher. ✉e-mail: frolov2@llnl.gov; dehm@mpie.de; liebscher@mpie.de

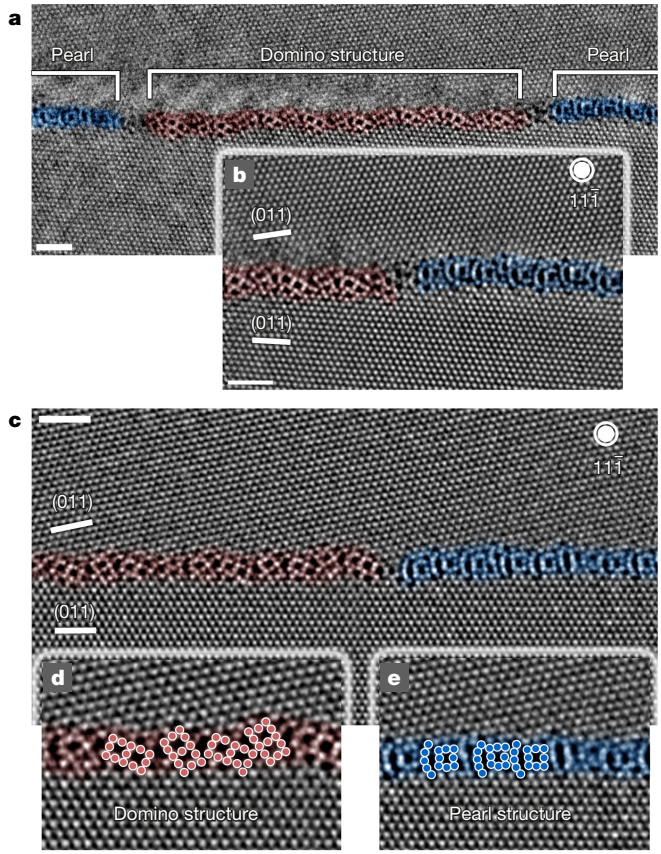

Fig. 1 | HAADF-STEM images of two congruent GB phase transitions. **a**, Overview image of the transition at a near-symmetric Σ19b [11$\bar{1}$] GB with (178) boundary plane. The domino and pearl structures (or GB phases) are highlighted in red and blue, respectively. The overall misorientation of the GB is about 48°, with a deviation in inclination from the symmetric orientation of about 1°. **b**, Magnified view of the GB transition on the right, highlighting the differences in structural units of both boundary segments. **c**, GB phase transition at a vicinal Σ19b [11$\bar{1}$] GB with approximately 47° misorientation and boundary planes of (011) for the lower grain and (279) for the upper grain. Panels **d** and **e** illustrate close-up images of the domino and pearl structure of the vicinal boundary, respectively. The scale bar is 1 nm in all images.

GB structure search

To investigate the structure and properties of the domino and pearl GB phases and to model the structural transformations revealed by the experiment, we performed GB structure search using atomistic calculations. The 0 K GB structure search was performed using an evolutionary algorithm based on the USPEX code[21,25,26]. The details of the method are described in the Methods and in ref. [21]. The results of the evolutionary search and clustering analysis of Σ19b (178) [11$\bar{1}$] GBs are illustrated in Fig. 2. The GB energy of hundreds of generated structures is plotted as a function of the number of inserted atoms n, measured as a fraction of the bulk (178) plane parallel to the GB introduced in ref. [20], as shown in Fig. 2a. The lowest-energy configuration predicted by our search is identified as the pearl structure, similar to what is observed in the experiment. Its structure is shown in Fig. 3a, b. This ground state is located at $n = 0$, which means that the insertion or removal of atoms is not necessary. No other minima with different n are present, suggesting the absence of competing GB phases with higher atomic density. To identify possible metastable states, we performed clustering analysis following the methodology proposed in ref. [21]. In this approach, the excess thermodynamic properties are used as descriptors to cluster similar GB structures and separate distinct GB phases that are expected to have different properties. Figure 2b shows the excess GB volume $[V]_N$ plotted against one of the components of the excess GB stress τ_{11} (where N is the number of atoms and the square brackets indicate an excess of the quantity measured per unit of GB area). The plot reveals two clusters that we automatically labelled using the k-means clustering algorithms. The blue cluster contains the ground state, as seen in the inset of Fig. 2b, and corresponds to pearl-like structures, while the red cluster represents metastable GB phases relative to pearl. The examination of structures in the red cluster established that they belong to the domino phase and the inset of Fig. 2b shows the lowest-energy configuration. By re-plotting the GB energy of the clustered data as a function of inserted atoms, it becomes apparent that the lowest-energy configuration within the domino-like structures has the same number of atoms $n = 0$ as the pearl-phase ground state, which is indicated by arrows in Fig. 2d. This analysis suggests that the structural transformation between the pearl and domino GB phases is not limited by the supply of vacancies or interstitials.

Although the two GB phases have the same number of atoms with energies differing only by about 4% ($\gamma_{\text{pearl}} = 0.835\,\text{J m}^{-2}$, $\gamma_{\text{domino}} = 0.871\,\text{J m}^{-2}$), they can clearly be distinguished by other thermodynamic properties reported in Extended Data Table 1. The excess volumes per unit area of the lowest-energy pearl and domino GB structures differ by about 36% and the GB stress of the two phases is not only different, but even has an opposite sign, indicating that the experimentally observed transition is of first order. The difference in the excess properties can be used to predict strains and stresses to stabilize the metastable domino phase (see Methods) as shown in Extended Data Fig. 7. At 0 K, 2% lateral strain, about 5 GPa of tensile stress or 440 MPa of shear stress can stabilize the domino phase in our model. The structural units of the lowest-energy pearl and domino phases projected along the [11$\bar{1}$] tilt axis and viewed along [5$\bar{3}$2] are illustrated in Fig. 3.

Simulations of GB transformations

The evolutionary search produces zero-temperature structures and we now turn to finite-temperature molecular dynamics (MD) simulations to investigate the high-temperature GB behaviour and phase transitions. Our goal was to reproduce the experimentally observed transition between the pearl and domino GB phases and to gain insight into the kinetics of the transformation to explain the room-temperature stability of the two-phase states found in both the symmetric and asymmetric boundaries. We simulated pearl and domino GB structures separately at temperatures ranging from 300 K to 900 K using simulation blocks with periodic boundary conditions along the GB as well as blocks with boundaries terminated at an open surface (see Methods). Our simulations demonstrated that in our model system at ambient pressure the pearl structure remained the ground state at all temperatures studied. The domino structure was metastable and transformed into pearl by nucleation and growth, characteristic of first-order transitions. In agreement with the predictions of the 0 K search, these simulations confirmed that the number of atoms at the GB does not change upon the transformation, that is, the transformation is diffusionless. Figure 4a shows the simulation block after an initially uniform domino GB phase was annealed for several nanoseconds. The pearl GB phase nucleated at both open surfaces and grew inwards, transforming the parent domino GB phase. The two structures are separated by a GB phase junction: a line defect that separates the two structures as highlighted in Fig. 4b. The two-phase structure shown in Fig. 4c closely resembles the experimentally observed GB transition illustrated in Fig. 4d.

We also found that the velocity of the GB phase junction, which determines the rate of the transformation, strongly depends on temperature and the defect length along the periodic dimension y, the [11$\bar{1}$] tilt axis. At relatively high temperatures, such as 650 K, a complete transformation of the GB structure (Fig. 4) can occur within a few tens of nanoseconds. Further simulations (see Methods) with different sizes of the

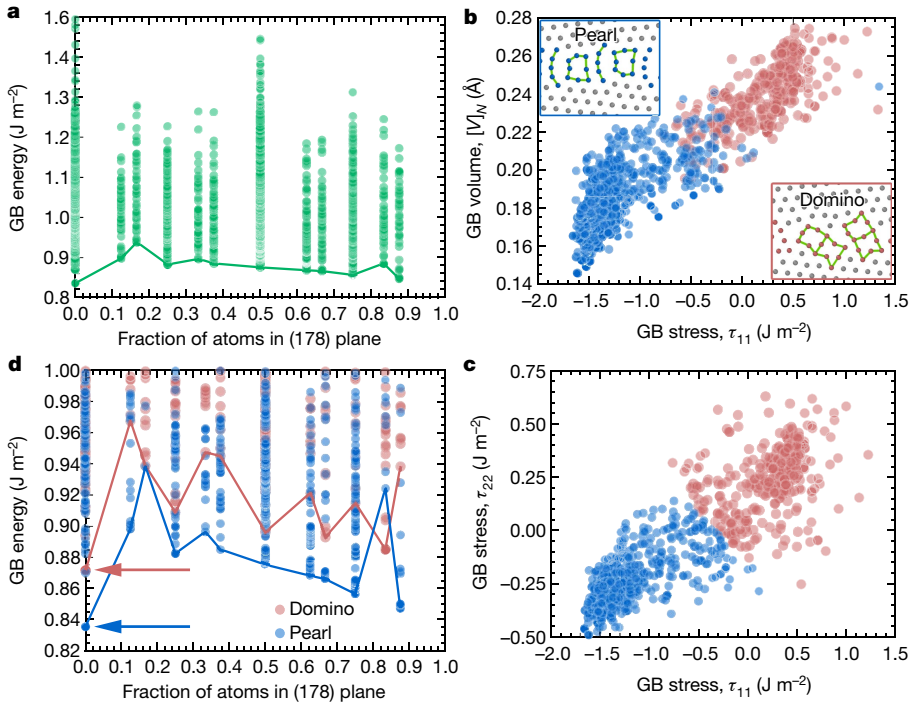

Fig. 2 | Evolutionary GB structure search and clustering analysis predicts the pearl and domino GB phases of the Σ19b (178)[11$\bar{1}$] GBs. **a**, GB energy of the structures generated plotted versus the number of inserted atoms calculated as a fraction of the (178) bulk plane. The solid line connects the lowest-energy structures with different numbers of atoms. **b**, Excess volume of the structures generated plotted versus excess GB stress τ_{11}. **c**, Excess GB stress τ_{22} of the generated structures plotted versus excess GB stress τ_{11}. The two clusters in the space of GB properties $[V]_N$, τ_{11} and τ_{22} were automatically identified using the *k*-means clustering algorithm. The two clusters coloured in blue and red correspond to the pearl and domino phases, respectively. The lowest-energy structures of the domino and pearl phases are given as insets in **b**. **d**, GB energy versus the number of atoms, as in **a**, with points assigned to the pearl or domino phase. The arrows indicate the ground-state structures of the pearl and domino phases, respectively. The lowest-energy configurations have the same number of atoms.

simulation block indicate that the motion of the GB phase junction is length-dependent, suggesting that it migrates by a kink nucleation mechanism, similar to dislocations. The nucleation barrier of this thermally activated process is apparently high enough to kinetically trap the two-phase coexisting state on the MD timescale at room temperature. When the length of the GB phase junction exceeds a few nanometres, we observe no migration of the junction at temperatures of 500 K and below. These simulations suggest that the experimentally observed two-phase states do not have to be in thermodynamic equilibrium at room temperature, but are instead kinetically trapped.

To study the effect of temperature on the relative stability of domino and pearl phases we performed free energy calculations following the methodology of refs. [31,32]. The results of the calculations as shown in Extended Data Fig. 8 confirm that the free energy difference decreases by 30% from 0 K to 800 K, bringing the phases closer to coexistence. We also demonstrate that equilibrium phase coexistence and reverse transformations can be observed in our model when tensile stresses of around 3.3 GPa or shear stresses in the range 200–350 MPa are applied at 500 K (see Extended Data Fig. 9).

Atomic-scale experimental observations of GB phase coexistence and transformations at symmetric and asymmetric tilt GBs in pure metallic systems have not been previously reported. Atomic resolution imaging reveals that the two coexisting GB phases are distinct, with different structural repeat units. In contrast to assumptions based on thermodynamic concepts[4], GB phase coexistence is also observed at an asymmetric GB. This indicates that GB phase transitions in pure systems can also emerge at more general boundaries and thus may strongly influence materials properties. It is the combination of atomic-scale observations and structure prediction that reveals that the GB phases

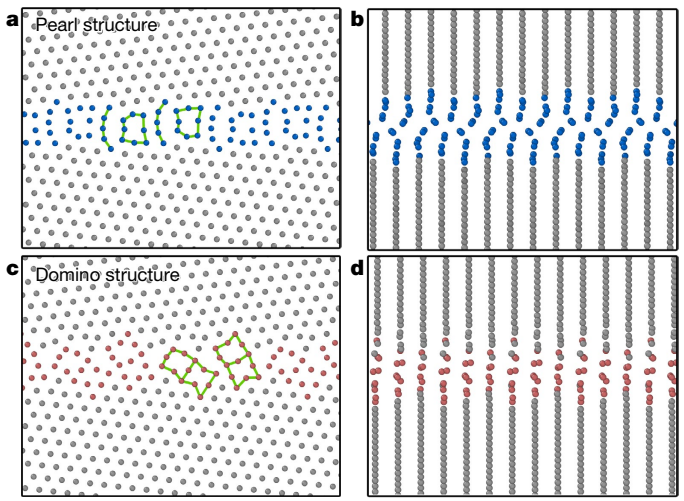

Fig. 3 | Structures of the pearl and domino GB phases predicted by the evolutionary search. **a** and **c** show projections along the [11$\bar{1}$] tilt axis of the pearl and domino phases, respectively. **b** and **d** visualize the GB structures perpendicular to the tilt axis viewed along [5$\bar{3}$2].

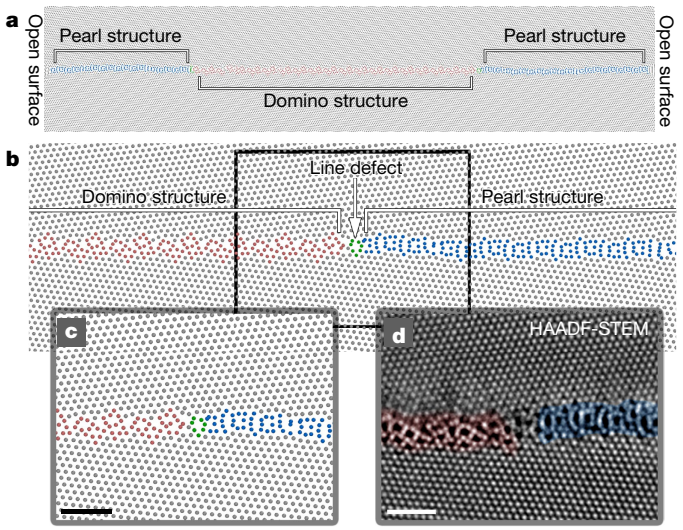

Fig. 4 | Simulated GB phase transition at finite temperature. **a**, MD simulation cell with open surfaces of a Σ19b (178)[11$\bar{1}$] tilt GB viewed along the tilt axis. The domino phase is highlighted in red, and the pearl phase in blue. **b**, Close up of the right-side phase transition with an indication of the GB phase junction (line defect, green), separating the two GB phases. **c**, Magnified view of the line defect and phase coexistence of the domino and pearl phases. **d**, Experimental HAADF-STEM image of the symmetric GB phase transition shown in Fig. 1b. The scale bar is 1 nm.

differ in excess thermodynamic properties and that their transformation is kinetically limited.

Our GB structure search predicted both experimentally observed pearl and domino GB phases in the symmetric and asymmetric boundaries. Interestingly, the calculations showed that both GB phases have the same number of atoms, suggesting that the stability of the two-phase states seen in the experiment and simulations at room temperature cannot be explained by the need to supply atoms by diffusion. The differing excess properties of the GB phases predicted by the calculations are expected to have a strong effect on GB properties such as diffusion, segregation or crack healing[20,29,33]. Furthermore, the core structure and energies of disconnections of the GB phases might differ, which should affect disconnection nucleation and hence GB migration.

Our high-temperature MD simulations of the GB phase transition reproduce the experimentally observed GB phases (see Figs. 1, 4). The strong dependence of the transformation rate on temperature and the GB phase junction length suggests that the motion of GB phase junctions may require the nucleation of kink pairs and could impede the transformation at low temperatures.

The experimental observation of the coexistence of two distinct GB phases at room temperature can thus be rationalized in terms of temperature-induced GB phase transformations and retarded transformation kinetics. During cooling to room temperature, the domino GB phase starts transforming into the pearl phase by nucleation. The steadily decreasing mobility of the GB phase junction eventually freezes isolated domino GB phase regions at temperatures below approximately 500 K, making their observation possible in the experiment. Previously, a similar trapping has been demonstrated only in multicomponent, glass-forming alloys[34]. In addition, the difference in excess properties of the domino and pearl phases suggests that stresses could potentially contribute to the stability of the domino phase. This is supported by modelling finite-temperature coexistence of the GB phases at 500 K under tensile stresses of around 3.3 GPa and σ_{23} shear stresses of 200–350 MPa (see Methods). Although the gigapascal-level tensile stresses are too high to be supported by the real material, the shear stresses are comparable to local shear stresses observed in previous experiments[35]. Furthermore, it implies that in addition to temperature, shear stresses have a much stronger effect on the free energy difference than tensile stresses. Hence, we cannot rule out that stresses of few hundred megapascals potentially present in the material could also influence the experimentally observed GB phase coexistence.

Conventional phase transitions in the bulk control many materials properties. Much of materials science involves the delicate interweaving of thermodynamics and kinetics, using phase transitions to sculpt advantageous microstructures. Although GB kinetics have long been understood to be key to attaining favourable grain structures, the possible role of GB phase transitions has been neglected. They had not been studied in metals because none had been observed. The recent suggestions of modelling[20,21,23] and now the discovery of GB phase transitions in a relatively simple elemental metal suggest novel strategies for materials design.

Online content

Any methods, additional references, Nature Research reporting summaries, source data, extended data, supplementary information, acknowledgements, peer review information; details of author contributions and competing interests; and statements of data and code availability are available at https://doi.org/10.1038/s41586-020-2082-6.

1. Sutton, A. P. & Balluffi, R. W. *Interfaces in Crystalline Materials* (Clarendon Press, 1995).
2. Hart, E. W. Two-dimensional phase transformation in grain boundaries. *Scr. Metall.* **2**, 179–182 (1968).
3. Hart, E. W. *The Nature and Behavior of Grain Boundaries* 155–170 (Springer, 1972).
4. Cahn, J. W. Transitions and phase equilibria among grain boundary structures. *J. Phys. Colloq.* **43**, 199–213 (1982).
5. Rottman, C. Theory of phase transitions at internal interfaces. *J. Phys. Colloq.* **49**, 313–326 (1988).
6. Han, J., Vitek, V. & Srolovitz, D. J. Grain-boundary metastability and its statistical properties. *Acta Mater.* **104**, 259–273 (2016).
7. Tang, M., Carter, W. C. & Cannon, R. M. Diffuse interface model for structural transitions of grain boundaries. *Phys. Rev. B* **73**, 024102 (2006).
8. Dillon, S. J., Tang, M., Carter, W. C. & Harmer, M. P. Complexion: a new concept for kinetic engineering in materials science. *Acta Mater.* **55**, 6208–6218 (2007).
9. Luo, J., Cheng, H., Asl, K. M., Kiely, C. J. & Harmer, M. P. The role of a bilayer interfacial phase on liquid metal embrittlement. *Science* **333**, 1730–1733 (2011).
10. Cantwell, P. R. et al. Grain boundary complexions. *Acta Mater.* **62**, 1–48 (2014).
11. Udler, D. & Seidman, D. N. Congruent phase transition at a twist boundary induced by solute segregation. *Phys. Rev. Lett.* **77**, 3379–3382 (1996).
12. Duscher, G., Chisholm, M. F., Alber, U. & Rühle, M. Bismuth-induced embrittlement of copper grain boundaries. *Nat. Mater.* **3**, 621–626 (2004).
13. Schweinfest, R., Paxton, A. T. & Finnis, M. W. Bismuth embrittlement of copper is an atomic size effect. *Nature* **432**, 1008–1011 (2004).
14. Tang, M., Carter, W. C. & Cannon, R. M. Grain boundary transitions in binary alloys. *Phys. Rev. Lett.* **97**, 075502 (2006).
15. Dillon, S. J., Harmer, M. P. & Luo, J. Grain boundary complexions in ceramics and metals: an overview. *JOM* **61**, 38–44 (2009).
16. Wang, Z. et al. Atom-resolved imaging of ordered defect superstructures at individual grain boundaries. *Nature* **479**, 380–383 (2011).
17. Rohrer, G. S. The role of grain boundary energy in grain boundary complexion transitions. *Curr. Opin. Solid State Mater. Sci.* **20**, 231–239 (2016).
18. Zhou, N., Hu, T. & Luo, J. Grain boundary complexions in multicomponent alloys: Challenges and opportunities. *Curr. Opin. Solid State Mater. Sci.* **20**, 268–277 (2016).
19. Yu, Z. et al. Segregation-induced ordered superstructures at general grain boundaries in a nickel-bismuth alloy. *Science* **358**, 97–101 (2017).
20. Frolov, T., Olmsted, D. L., Asta, M. & Mishin, Y. Structural phase transformations in metallic grain boundaries. *Nat. Commun.* **4**, 1899 (2013).
21. Zhu, Q., Samanta, A., Li, B., Rudd, R. E. & Frolov, T. Predicting phase behavior of grain boundaries with evolutionary search and machine learning. *Nat. Commun.* **9**, 467 (2018).
22. Carrion, F., Kalonji, G. & Yip, S. Evidence for grain boundary phase transition in a 2D bicrystal. *Scr. Metall.* **17**, 915–918 (1983).
23. Frolov, T. et al. Grain boundary phases in bcc metals. *Nanoscale* **10**, 8253–8268 (2018).
24. Chua, A. L., Benedek, N. A., Chen, L., Finnis, M. W. & Sutton, A. P. A genetic algorithm for predicting the structures of interfaces in multi-component systems. *Nat. Mater.* **9**, 418–422 (2010).
25. Oganov, A. R. & Glass, C. W. Crystal structure prediction using ab initio evolutionary techniques: principles and applications. *J. Chem. Phys.* **124**, 244704 (2006).
26. Lyakhov, A. O., Oganov, A. R., Stokes, H. T. & Zhu, Q. New developments in evolutionary structure prediction algorithm USPEX. *Comput. Phys. Commun.* **184**, 1172–1182 (2013).
27. Maksimova, E. L., Shvindlerman, L. S. & Straumal, B. B. Transformation of Σ17 special tilt boundaries to general boundaries in tin. *Acta Metall.* **36**, 1573–1583 (1988).
28. Rabkin, E., Minkwitz, C., Herzig, C. H. & Klinger, L. Evidence for structural multiplicity of the Σ = 3 incoherent twin boundary in Cu from grain-boundary diffusion measurements. *Phil. Mag. Lett.* **79**, 409–415 (1999).
29. Divinski, S. V., Edelhoff, H. & Prokofjev, S. Diffusion and segregation of silver in copper Σ5(310) grain boundary. *Phys. Rev. B* **85**, 144104 (2012).
30. Dehm, G., Edongué, H., Wagner, T., Oh, S. H. & Arzt, E. Obtaining different orientation relationships for Cu films grown on (0001) α-Al2O3 substrates by magnetron sputtering. *Z. Metall. Mater. Res. Adv. Techniq.* **96**, 249–254 (2005).
31. Freitas, R., Asta, M. & de Koning, M. Nonequilibrium free-energy calculation of solids using LAMMPS. *Comput. Mater. Sci.* **112**, 333–341 (2016).
32. Freitas, R., Rudd, R. E., Asta, M. & Frolov, T. Free energy of grain boundary phases: atomistic calculations for Σ5(310)[001] grain boundary in Cu. *Phys. Rev. Mater.* **2**, 093603 (2018).
33. Aramfard, M. & Deng, C. Mechanically enhanced grain boundary structural phase transformation in Cu. *Acta Mater.* **146**, 304–313 (2018).
34. Khalajhedayati, A., Pan, Z. & Rupert, T. J. Manipulating the interfacial structure of nanomaterials to achieve a unique combination of strength and ductility. *Nat. Commun.* **7**, 10802 (2016).
35. Phillips, M. A. et al. X-ray microdiffraction: local stress distributions in polycrystalline and epitaxial thin films. *Microelectron. Eng.* **75**, 117–126 (2004).

Methods

Cu thin films and transmission electron microscope (TEM) specimen preparation

The GB structures presented were obtained from Cu thin films grown by molecular beam epitaxy on (0001)-oriented sapphire substrates at room temperature with post-deposition annealing at 673 K for 3 h. The depositions were performed at the Central Scientific Facility Materials of the Max Planck Institute for Intelligent Systems in Stuttgart. The global grain structure of the thin film was analysed by electron backscatter diffraction in a JEOL JSM-6490 scanning electron microscope (SEM) (see Extended Data Fig. 1). The TEM specimens were extracted from specific locations of the thin film by an in-plane lift-out technique in a dual-beam SEM/focused ion beam instrument (Helios Nanolab 600i, Thermo Fisher Scientific).

The grain orientation, the distribution of coincident site lattice GBs and the corresponding inverse pole figure of the Cu thin films grown by molecular beam epitaxy is shown in Extended Data Fig. 1. All grains have a $[11\bar{1}]$ orientation, which is parallel to the growth direction of the thin film, ideally suited for atomic structure observations at room temperature. Most of the GBs are Σ3, Σ7, Σ19b and Σ37c with the $[11\bar{1}]$ tilt axis highlighted in black, yellow, red and green, respectively. The grain size is about 100 ± 50 μm with a bimodal distribution and the grains exhibit a cylindrical shape. Residual thermal tensile stresses of the order of 100 MPa are present in the annealed Cu thin film[36]. The shear stresses in similar thin films can show strong local variations even exceeding the average residual thermal stress[35]. The Σ19b used in this study is shown in red. The white rectangle in the centre of the example electron backscatter diffraction map shows a location where a TEM specimen was extracted by focused-ion-beam preparation.

Scanning transmission electron microscopy (STEM)

All STEM data were acquired using a probe corrected FEI Titan Themis 60-300 (Thermo Fisher Scientific). The TEM is equipped with a high-brightness field emission gun and a gun monochromator. The electrons were accelerated to 300 kV and images were recorded at a probe current of about 80 pA with a high-angle annular dark field (HAADF) detector (Fishione Instruments Model 3000). The collection angles for the HAADF images were set to 73–200 mrad using a semi-convergence angle of 23.8 mrad. Image series with 20–40 images and a dwell time of 1–2 μs were acquired, registered and averaged in order to minimize the effect of instrumental instabilities and noise in the images.

STEM multi-slice image simulations

STEM multi-slice simulations were performed by the Prismatic software[37,38]. The GB structures predicted by evolutionary search were used as input files for the image simulations to enable a direct comparison of simulation and experiment. The thickness of all simulated cells was set to 22 nm and a slice thickness of 0.2 nm was used. In total, 8 frozen phonon configurations were incoherently summed to include the thermal vibration of atoms. The pixel size was set to 10 pm. The microscope parameters, such as HAADF detector collection angles (73–200 mrad), semi-convergence angle (23.8 mrad) and primary electron energy (300 kV) were identical to the experimental values.

Structure prediction by evolutionary search and clustering at 0 K

Following the evolutionary approach, the algorithm samples a diverse population of different GB structures, while improving them over many generations on the basis of the energy minimization criterion. During the search, the structures change owing to heredity and mutations, and atoms are inserted and removed from the GB core to identify structures with different atomic densities. The search changes the GB periodic dimensions to also sample large-area reconstructions of the GB. The 0 K evolutionary search was evolved over 50 generations. The search sampled different atomic densities given as the number of atoms inserted into the boundary as a fraction of the (178) bulk plane, ranging from 0 to 1. Four independent evolutionary searches were performed. The GB cross-section was varied during the search between the smallest possible value and a cross-section four times as large. The LAMMPS code[39] was used to evaluate the energies of the generated structures. The GB structures were inspected and visualized with OVITO[40]. Viewing perpendicular to the tilt axis along $[5\bar{3}2]$ reveals that the lattice planes in the upper crystal appear to be shifted for the pearl phase (Fig. 3b), but remain continuous without any shift for the domino phase (Fig. 3d). The shift translation vector is inclined with respect to the image plane and is 1/6 [920].

Clustering analysis was performed to identify distinct GB phases, following the methodology proposed in refs. [20,21]. The excess properties including excess volume $[V]_N$ and two components of GB stress, τ_{11} and τ_{22}, were calculated for each structure generated. The excess volumes of the ground-state pearl structure and the lowest-energy domino structure are $[V]_{N,\mathrm{pearl}} = 0.14$ Å and $[V]_{N,\mathrm{domino}} = 0.22$ Å, respectively. The GB excess stresses of the ground-state pearl structure are determined to be $\tau_{11,\mathrm{pearl}} = -1.66\ \mathrm{J\,m^{-2}}$ and $\tau_{22,\mathrm{pearl}} = -0.46\ \mathrm{J\,m^{-2}}$ and for the lowest-energy domino structure to be $\tau_{11,\mathrm{domino}} = 0.25\ \mathrm{J\,m^{-2}}$ and $\tau_{22,\mathrm{pearl}} = 0.29\ \mathrm{J\,m^{-2}}$.

Prior to clustering, these features were scaled using the StandardScaler function implemented in the scikit-learn Python library (https://scikit-learn.org/). The clustering was performed using the *k*-means clustering algorithm, also implemented in the scikit-learn library.

Linking structure prediction and experimental observations

Atomic-resolution observations and atomistic predictions can be directly linked by multislice STEM image simulations[37,41]. The predicted GB structures served as input for STEM image simulations, to quantitatively compare atomic peak positions and intensities at the GB core of different pearl GB structures (see Extended Data Fig. 2). For this analysis, we selected three different pearl-like structures produced by the evolutionary search including the ground state, a higher-energy state with large atomic density as well as one poorly optimized configuration with high energy. The GB energy of pearl structures is plotted against the number of inserted atoms *n* as a fraction of the (178) GB plane in Extended Data Fig. 2a. The approximate locations of the input GB structures used for STEM image simulations in the plot are highlighted by red, green and yellow circles, respectively. In Extended Data Fig. 2b–d, the corresponding projections of the GB structures along the $[11\bar{1}]$ tilt axis and perpendicular to it are shown in the left and right panels, respectively. The ground-state structure of the pearl phase, as predicted by USPEX at 0 K, with a GB energy of $0.835\ \mathrm{J\,m^{-2}}$, is shown in Extended Data Fig. 2b (highlighted in red). The higher-energy structures with GB energies of $0.932\ \mathrm{J\,m^{-2}}$ (in green) and $1.023\ \mathrm{J\,m^{-2}}$ (in yellow) are illustrated in Extended Data Fig. 2c, d. Locations where atoms are displaced from their ideal positions with respect to the $[11\bar{1}]$ viewing direction are marked by arrows in Extended Data Fig. 2c. The atomic displacements in these regions lead to dechannelling of the electron probe and hence a reduction of the HAADF-STEM image intensity.

An atomic-resolution STEM image of the symmetric pearl structure and its structural unit are illustrated in Extended Data Fig. 3a. Visual inspection reveals excellent agreement with the predicted ground state of the pearl phase presented in Extended Data Fig. 2a. Since the atomic column peak intensity in aberration-corrected STEM is sensitive to the number of atoms in the column, the elemental species but also atomic displacements, it can be used to quantitatively compare experiment and simulation. In Extended Data Fig. 3b–e, only the peak intensities at the GB core are coloured. The experimental STEM image shown in Extended Data Fig. 3b agrees best with the simulated STEM image of the ground-state pearl structure illustrated in Extended Data Fig. 3c. The strong scatter in peak intensities in the simulated STEM images of Extended Data Fig. 3d, e is a result of pronounced displacement of atoms perpendicular to the $[11\bar{1}]$ beam direction. This inhomogeneous intensity distribution originates from the higher degree of disorder at

the GB core of these high-energy pearl structures. Thus, direct comparison of experiment and simulation at the atomic scale reveals excellent agreement, and shows that the experimentally observed pearl GB structure resembles a low-energy state.

Finite temperature MD simulations

MD simulations were performed using the LAMMPS code[39] in the canonical NVT ensemble with a Nose–Hoover thermostat. To model the transition from the metastable domino phase to the pearl phase, we performed independent isothermal simulations at temperatures ranging from 300 K to 900 K. We used blocks with periodic boundary conditions along the boundary as well as blocks with open surfaces. The open-surface simulation methodology was introduced in ref. [20] to allow for supply or outflow of atoms to the GB in case it should be necessary to achieve the ground state. Only periodic boundary conditions were used along the $[11\bar{1}]$ tilt axis. We used different sizes of the simulation block to investigate the effect of the GB phase junction length on the kinetics of the transformation. The simulated GB transitions were visualized with OVITO[40]. GB free energy calculations of the pearl and domino GB phases at ambient pressure were performed using harmonic and quasi-harmonic methods as described in refs. [31,32,42].

To model the transition from the metastable domino phase to the pearl phase, we performed independent isothermal simulations at temperatures of 300 K, 400 K, 500 K, 600 K, 650 K, 700 K, 800 K, 850 K and 900 K. We used blocks with periodic boundary conditions along the boundary as well as blocks with open surfaces. We also used different sizes of the simulation block to investigate the effect of the GB phase junction length on the kinetics of the transformation.

Symmetric tilt GBs with periodic boundary conditions

We used a simulation block with dimensions $33.6 \times 34 \times 14$ nm^3 containing 1,339,740 atoms. The z direction was normal to the GB plane. The simulations were performed for up to 200 ns. We observed a transformation of the domino phase to the pearl phase at 850 K and 900 K. At temperatures below 850 K, the initial domino phase remained stable and well ordered throughout the entire simulation. From these simulations, we estimated the limit of pearl phase stability to be around 900 K. The simulations also confirmed that a supply of atoms was not necessary to achieve the transformation.

Symmetric tilt GBs with open surface

When the boundary was terminated at an open surface, we were able to observe the transition from domino to pearl at much lower temperatures. In all of these simulations the pearl phase nucleated at the surface triple junctions. The simulations showed a strong effect of temperature on the kinetics of the transformation. The initial simulation block had dimensions of $45 \times 0.626 \times 14$ nm^3 and contained 33,080 atoms. Here, the y periodic dimension, which also defines the length of the GB phase junction, was only one periodic unit length along the $[11\bar{1}]$ direction $L_y = a_0 \times \sqrt{3} = 0.626$ nm. In these quasi-two-dimensional simulations, we were able to observe the nucleation of the pearl phase at 400 K, which was much lower compared to the homogeneous nucleation at 850 K in a block with periodic boundary conditions. However, after the pearl phase nucleated, the migration of the junction was too slow and we were not able to observe a complete transformation at this temperature. At 300 K we did not observe pearl phase nucleation at all. More rapid nucleation kinetics and complete transformations were observed at higher temperatures of 500 K, 600 K and 650 K. At 500 K, the full transformation was already completed, within only 13 ns of the simulation. During this time, the two GB junctions travel the distance of $L_x = 45$ nm. In principle, these simulations allow us to evaluate the velocity of the GB junction and, by approximating the driving force as the GB energy difference at 0 K, even the mobility of the GB phase junction at 300 K can be predicted on the experimental timescale. However, although these simulations with the artificially short dimension $L_y = 0.626$ nm allowed us to observe GB phase transitions at low temperatures, they are likely to overestimate the mobility of the GB phase junction.

To study the effects of the GB phase junction length, we increased the size L_y of the simulation block by replicating the initial block along the periodic direction y 40 times. The final dimensions of the simulation block were $45 \times 25 \times 14$ nm^3 and it contained 1,323,200 atoms. The initial configurations were taken from the middle of the 500 K simulation and contained both the pearl and the domino phases. We obtained the large simulation block for 200 ns at 500 K and did not observe any substantial migration of the GB phase junction. This behaviour was very different from a complete transformation at the same temperature in a thinner block, in which the GB phase junctions travelled the entire length L_x of 45 nm. In these simulations, we effectively froze the transformation at 500 K by making the GB phase junction longer. At higher temperatures such as 650 K, we observed a complete transformation again even in the thicker block during 48 ns of the simulation.

Asymmetric tilt GBs

The asymmetric boundary is 6° inclined relative to the symmetric orientation. Its periodic dimensions were substantially larger than that of the symmetric boundary. As a result, we did not attempt a full grand canonical optimization of the boundary with USPEX[21,25]. Instead, we used the common gamma-surface method which nevertheless generated both pearl and domino structures with energies of $\gamma_{gb} = 0.87$ J m^{-2} and 0.89 J m^{-2}, respectively. The different inclinations mean that the energy difference between the two structures reduces to 1.9%, which is even smaller than that for the symmetric GB. The structures of both asymmetric pearl and domino ground states are shown in Extended Data Fig. 4. Despite the smaller energy difference at 0 K, the pearl phase remains more stable at finite temperature for the asymmetric GB. MD simulations of a transformation from domino to pearl structure were performed at 600 K, 700 K, 800 K and 900 K using simulation blocks with dimensions $34 \times 2.5 \times 3.1$ nm^{3}containing 43,248 atoms. At these temperatures, we observed complete transformations to pearl phase as illustrated in Extended Data Fig. 5a, b. We intentionally used a relatively small size $L_z = 3.1$ nm to stabilize the asymmetric configuration. Interestingly, at a temperature of 600 K, the GB in the pearl structure remained asymmetric, while at all higher temperatures the symmetric configuration appears. The nucleation of the asymmetric pearl phase from the open surfaces at 700 K is shown in Extended Data Fig. 6a. The transformation from the initially asymmetric domino structure to the symmetric pearl phase is illustrated in Extended Data Fig. 6b.

Stabilizing the domino phase in atomistic simulations

Different phases of the same GB can have different entropies, so changing the temperature can change the relative free energies and induce a phase transformation. They can also have different excess volumes, excess stress and excess shears, so changing the stress and shear stress, respectively, can also induce transformation. Here we use thermodynamic analysis to identify conditions under which domino and pearl GB phases can coexist in equilibrium under non-hydrostatic conditions in the model. The analysis will predict strains and stresses that could stabilize the domino phase. At equilibrium coexistence the domino and pearl GB phases have the same free energies $\gamma_{domino} = \gamma_{pearl}$ (ref. [43]). Under general non-hydrostatic conditions the GB free energy of each phase is a function of temperature, lateral strains ε_{11}, ε_{12} and ε_{22} and stresses σ_{33} and σ_{23}, as described by the Gibbs adsorption equation[44]:

$$\mathrm{d}\gamma = -[S]_N \mathrm{d}T - [V]_N \mathrm{d}\sigma_{33} - [B]_N \mathrm{d}\sigma_{23} + \sum_{i,j=1,2} (f_{ij} - \delta_{ij}\gamma)\mathrm{d}\varepsilon_{ij} \qquad (1)$$

where $[S]_N$ is excess entropy, $[V]_N$ is excess volume, $[B]_N$ is excess shear, f_{ij} is excess GB stress and γ is given by[45]:

$$\gamma = [U]_N - T[S]_N - \sigma_{33}[V]_N - \sigma_{23}[B]_N \quad (2)$$

Just like the excess volume $[V]_N$, the excess shear $[B]_N$ represents extra displacement due to the boundary but in the direction of the tilt axis instead of normal to the boundary plane.

For the tilt GBs studied here we consider only shear stress σ_{23}, which is parallel to the boundary plane and is applied in the direction of the tilt axis. Non-zero σ_{13} leads to GB migration by coupled motion, breaking the thermodynamic equilibrium between the grains. As a result we restrict the equilibrium analysis to the non-hydrostatic states when σ_{13} is zero.

At 0 K we calculated γ_{domino} and γ_{pearl} directly by independently varying ε_{11}, σ_{33} and σ_{23} following the methodology described in ref. [45]. We focus on these variables because the corresponding GB excess volume, shear and stress f_{11} have the largest difference for the pearl and domino phases. Extended Data Fig. 7 shows that the curves cross at about $\varepsilon^*_{11} = -2\%$, $\sigma^*_{33} = 5$ GPa, and $\sigma^*_{23} = 0.44$ GPa, where the asterisk refers to coexistence conditions. These coexistence stresses and strains can also be estimated using equations (1) and (2) as follows: $\sigma^*_{33} \approx \Delta[U]_N/\Delta[V]_N$, $\sigma^*_{23} \approx \Delta[U]_N/\Delta[B]_N$, $\varepsilon^*_{11} \approx -\Delta[U]_N/\Delta(f_{11} - \gamma)$, where Δ refers to the difference between excess energy, stress, volume and shear of the pearl and domino phases at ambient conditions. For example, using our 0 K values, $\Delta[U]_N = [U]_{N,\text{domino}} - [U]_{N,\text{pearl}} = 0.835\,\text{J m}^{-2} - 0.871\,\text{J m}^{-2} = 0.036\,\text{J m}^{-2}$ and $\Delta[V]_N = [V]_{N,\text{domino}} - [V]_{N,\text{pearl}} = 0.22\,\text{Å} - 0.14\,\text{Å} = 0.08\,\text{Å}$, we estimate the tensile stress required to stabilize domino to be $\sigma_{33} \approx 4.5$ GPa, which closely matches the direct 0 K calculation shown in Extended Data Fig. 7b.

At finite temperature we can also estimate the strains and stresses required to achieve coexistence by using free energies $[U]_N - T[S]_N$, which we obtained from free energy calculations, instead of just $[U]_N$. Since the free energy difference decreased with temperature according to our calculations, shown in Extended Data Fig. 8, smaller stresses and strains should be required to bring the two phases to the equilibrium coexistence. For example, at 500 K and zero stress the free energy difference $\Delta[U - TS]_N = [U - TS]_{N,\text{domino}} - [U - TS]_{N,\text{pearl}} = 0.028\,\text{J m}^{-2}$ was obtained using harmonic approximation. Taking the excess volume difference $\Delta[V]_N = [V]_{N,\text{domino}} - [V]_{N,\text{pearl}} = 0.08$ Å we estimate the coexistence tensile stress $\sigma^*_{33} \approx 3.5$ GPa, which is smaller than the 0 K value. For lateral compression, similar analysis predicts GB phase coexistence at compressive strain $\varepsilon^*_{11} \approx \Delta[U - TS]_N/\Delta(f_{11} - \gamma) = 0.028\,\text{J m}^{-2}/(-0.621\,\text{J m}^{-2} + 2.495\,\text{J m}^{-2}) = -1.5\%$. Finally, we estimate shear stress parallel to the GB plane and in the direction of the tilt axis that should stabilize the domino phase as $\sigma^*_{23} \approx \Delta[U - TS]_N/\Delta[B]_N = 0.028\,\text{J m}^{-2}/(0.22\,\text{Å} - 0.98\,\text{Å}) = -360$ MPa.

GB phase transformations and coexistence under stress

To test the predicted values of stress required to establish equilibrium coexistence between pearl and domino GB phases we perform MD simulations at 500 K (see Extended Data Fig. 9). Here we focus on the coexistence due to stresses σ_{33} and σ_{23} in two separate sets of simulations. To demonstrate equilibrium and avoid hysteresis due to nucleation, we follow the methodology commonly employed in simulations of bulk phases: we start with a simulation block containing both GB phases and then monitor the motion of the GB phase junction. At coexistence, the junction is expected to fluctuate by performing random walk, while away from the coexistence we expect to observe growth of one of the phases. The growth simulations are particularly important to rule out false coexistence due to slow kinetics of the GB junction. We used periodic boundary conditions parallel to the GB plane. Along the z direction the boundary conditions were not periodic: free atoms were sandwiched between two 20-Å-thick surface layers. The boundary atoms were used to manipulate the stress state in the system. The simulation block had dimensions $100 \times 1.2 \times 14\,\text{nm}^3$ and contained 165,110 atoms.

Coexistence and transformations under tensile stress σ_{33}

We took the initial structure with two GB phases and applied tensile strain to generate stress in the cell. We performed separate simulations with stresses $\sigma_{33} = 3.95$ GPa, 3.3 GPa, 2.85 GPa and 0 GPa. The tensile stress was maintained by fixing the z coordinates on the 20-Å-thick top boundary surface layer and fixing the bottom boundary layer of the same thickness. At the same time we allowed displacements of the atoms in the top boundary layer in the x and y directions so that the σ_{13} and σ_{23} stresses remained zero. Similar to ambient pressure simulations at $\sigma_{33} = 2.85$ GPa, we observed growth of the pearl phase, indicating that this tensile stress was not sufficient to stabilize the domino phase. The reverse transformation was observed at $\sigma_{33} = 3.95$ GPa. Extended Data Fig. 9c shows that domino phase grew during 400 ns at the expense of the pearl phase, suggesting that this stress is above the GB phase coexistence. Finally, in the simulation at $\sigma_{33} = 3.3$ GPa we did not observe substantial growth of either of the phases, indicating that this stress is close to the coexistence value. This value agrees well with predictions based on the free energy calculations and thermodynamic analysis.

Coexistence and transformations under shear stress σ_{23}

To implement the simulations under shear stress conditions, we took the same initial configuration that we used before applying the tensile stress and ran a relatively short simulation with the bottom boundary layer of atoms fixed, while the top boundary layer of atoms was moved in small increments in the direction parallel to the tilt axis. During this simulation the shear stress increased to about 450 MPa and we saved snapshots that corresponded to different values of shear stress. The boundary atoms were allowed to move in the x and z direction so that σ_{13} and σ_{33} stresses remained zero. We then started independent simulations from different snapshots to study GB behaviour under shear stresses of 200, 300, 350 and 400 MPa. Extended Data Fig. 9d shows the substantial growth of the domino phase at about 350 MPa, suggesting that this value of stress stabilizes the domino phase above coexistence. At 200 MPa and 300 MPa we observed very small fluctuations of the position of the GB phase junction and no apparent growth of one of the phases. Based on these observations we conclude that the coexistence shear stress is between 200 MPa and 350 MPa, which is also consistent with our estimates based on the free energy calculations and thermodynamic analysis.

Data availability

Datasets generated or analysed during the current study are available in Edmond (the Open Access Data Repository of the Max Planck Society) under https://edmond.mpdl.mpg.de/imeji/collection/zV4i2cu2blAI8B. All other datasets are available from the corresponding authors on reasonable request.

36. Dehm, G., Balk, T. J., Edongué, H. & Arzt, E. Small-scale plasticity in thin Cu and Al films. *Microelectron. Eng.* **70**, 412–424 (2003).
37. Pryor, A., Ophus, C. & Miao, J. A streaming multi-GPU implementation of image simulation algorithms for scanning transmission electron microscopy. *Adv. Struct. Chem. Imaging* **3**, 15 (2017).
38. Ophus, C. A fast image simulation algorithm for scanning transmission electron microscopy. *Adv. Struct. Chem. Imaging* **3**, 13 (2017).
39. Plimpton, S. Fast parallel algorithms for short-range molecular dynamics. *J. Comput. Phys.* **117**, 1–19 (1995).
40. Stukowski, A. Visualization and analysis of atomistic simulation data with OVITO—the open visualization tool. *Model. Simul. Mater. Sci. Eng.* **18**, 015012 (2010).
41. Peter, N. J. et al. Segregation-induced nanofaceting transition at an asymmetric tilt grain boundary in copper. *Phys. Rev. Lett.* **121**, 255502 (2018).
42. Foiles, S. M. Evaluation of harmonic methods for calculating the free energy of defects in solids. *Phys. Rev. B* **49**, 14930–14938 (1994).
43. Gibbs, J. W. *The Collected Work of J. William Gibbs* Vol. 1 (Longmans, Green and Co., 1928).
44. Frolov, T. & Mishin, Y. Thermodynamics of coherent interfaces under mechanical stresses. I. Theory. *Phys. Rev. B* **85**, 224106 (2012).
45. Frolov, T. & Mishin, Y. Thermodynamics of coherent interfaces under mechanical stresses. II. Application to atomistic simulation of grain boundaries. *Phys. Rev. B* **85**, 224107 (2012).

Acknowledgements We thank G. Richter and his team from the Max Planck Institute for Intelligent Systems for producing the Cu thin films by molecular beam epitaxy. T.F. is grateful to R. Freitas for the help with the free energy calculations. G.D. and T.M. acknowledge financial support from the European Research Council through grant number 787446 GB-CORRELATE. Support for T.F. and R.E.R. was provided under the auspices of the US Department of Energy by Lawrence Livermore National Laboratory under contract DE-AC52-07NA27344. T.F. and R.E.R. were funded by the Laboratory Directed Research and Development Program at Lawrence Livermore National Laboratory under Project Tracking Code number 19-ERD-026.

Author contributions T.F., G.D. and C.H.L. supervised the project. T.M. characterized the samples, performed all microscopy measurements and conducted the STEM image simulations. T.M., G.D. and C.H.L. analysed the experimental and simulated microscopy data. T.F. performed GB structure search, data analysis, MD simulations and the thermodynamic analysis. T.F., T.M. and C.H.L. analysed the simulated GB data. T.M., C.H.L., T.F., R.E.R. and G.D. wrote the manuscript.

Competing interests The authors declare no competing interests.

Additional information

Correspondence and requests for materials should be addressed to T.F., G.D. or C.H.L.

Peer review information *Nature* thanks Eugen Rabkin, Gregory S. Rohrer and the other, anonymous, reviewer(s) for their contribution to the peer review of this work.

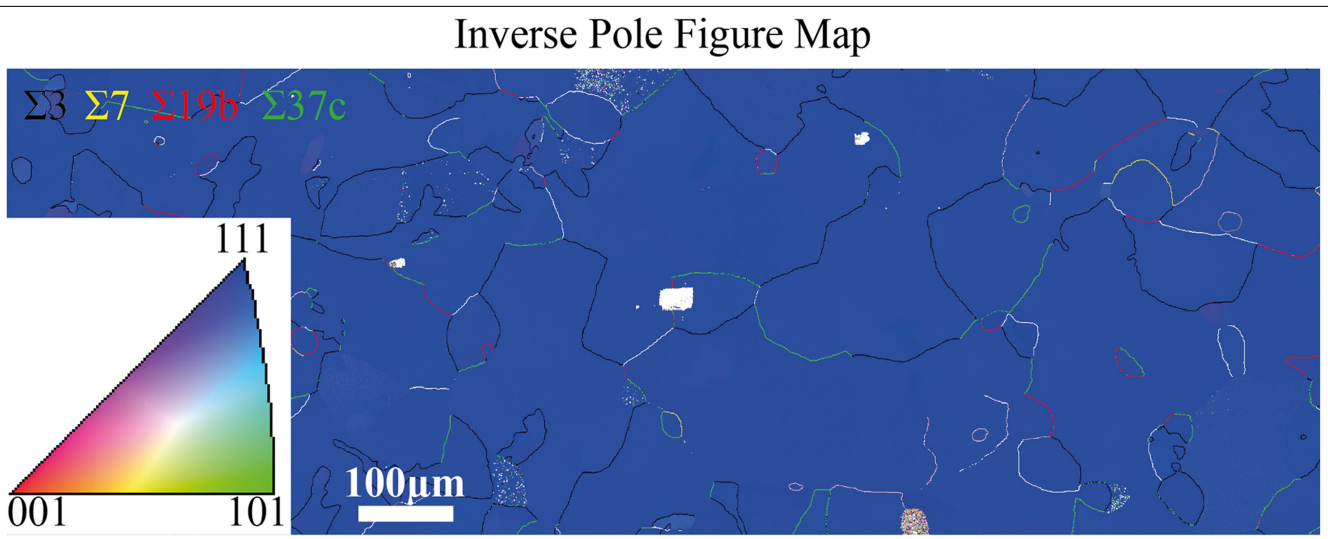

Extended Data Fig. 1 | Electron backscatter diffraction characterization of the Cu thin film. The [11$\bar{1}$] tilt GBs have been obtained by thin-film deposition of Cu on a (0001)-oriented sapphire substrate. The inverse pole figure shows that all grains are in the ⟨111⟩ orientation with an average grain size of ≤100 µm. The majority of GBs in the film are twin and low-angle GBs (up to 70%), but crucially, Σ7, Σ19b, Σ37c and the corresponding asymmetric boundaries are also present. The most prominent GBs are coloured. The Σ19b GBs are highlighted in red. The white rectangle in the centre shows a position where a TEM specimen has been extracted.

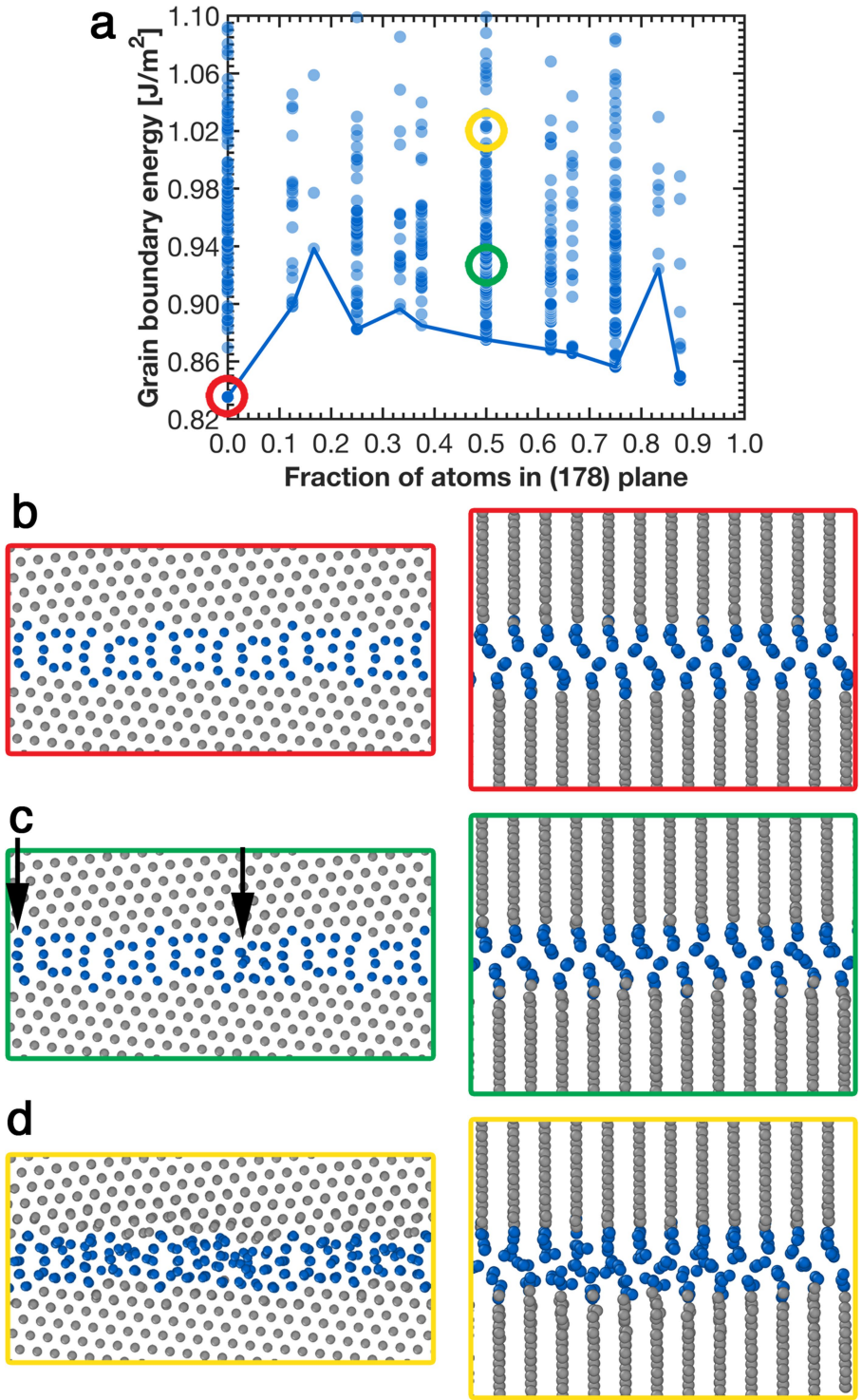

Extended Data Fig. 2 | Input GB structures for STEM image simulations. a, GB energy plotted versus the number of inserted atoms *n* as a fraction of the (178) GB plane. The red, green and yellow circles indicate the locations of the GB structures shown in **b**–**d**, which show the three GB structures used for STEM image simulation, respectively. Each left panel shows the structure along the tilt axis [11$\bar{1}$], and each right panel shows the structure perpendicular to the tilt axis. The coloured boxes indicate where these structures are located in the energy plot.

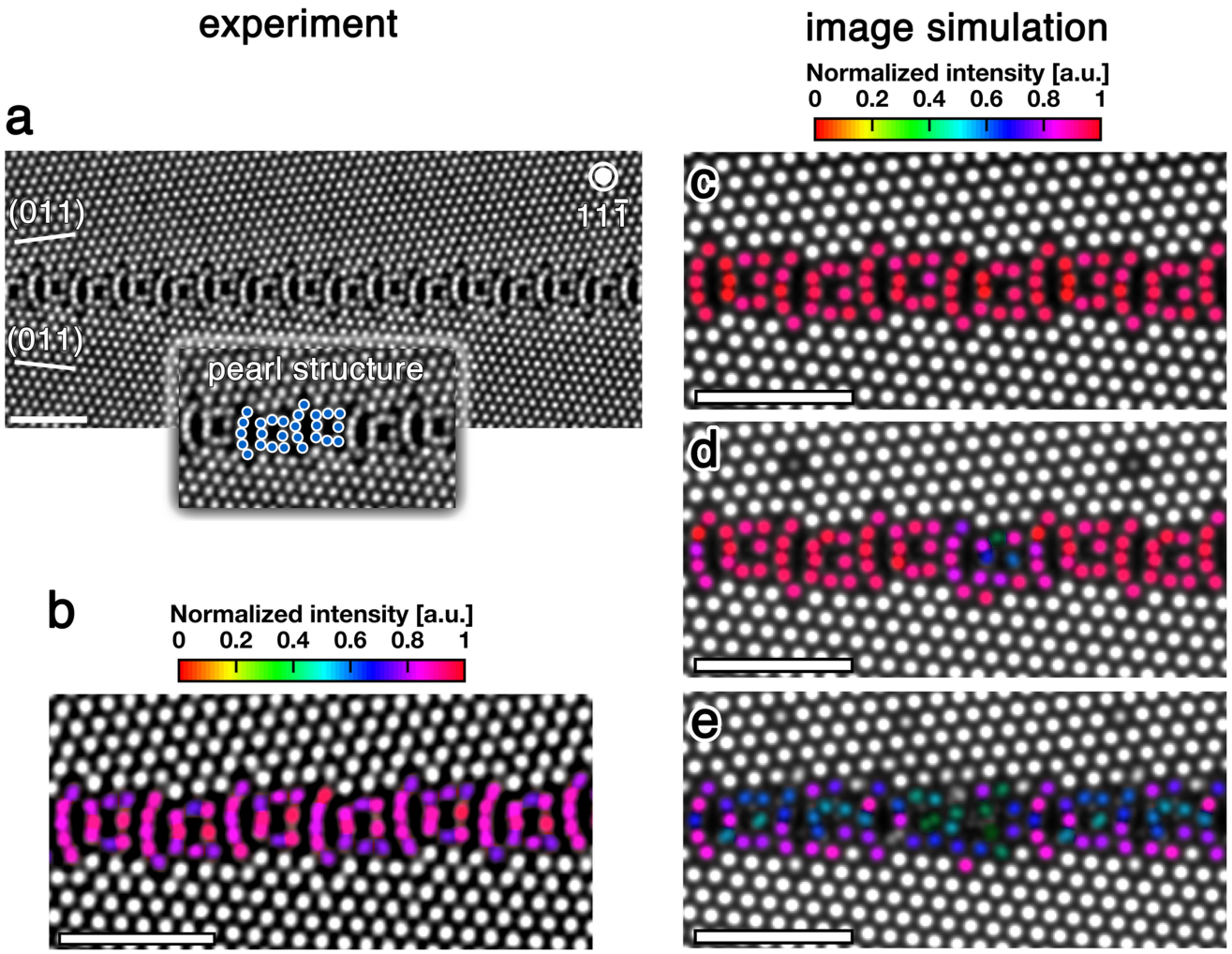

Extended Data Fig. 3 | Linking atomic-resolution observations and structure prediction. a, Aberration-corrected HAADF-STEM image of the symmetric Σ19b (178) [11$\bar{1}$] pearl phase. Its structural unit is highlighted in the inset. **b**, Colour coding of the experimental GB structure based on atomic column peak intensities. **c**–**e**, Simulated STEM images of the predicted GB structures by USPEX for a sample thickness of 22 nm. Colour coding as in **b**. **c**, Lowest-energy structure with GB energy of 0.835 J m^{-2} and $n = 0$; **d**, medium-energy GB structure with 0.932 J m^{-2} and $n = 0.5$; and **e**, high-energy GB structure with 1.023 J m^{-2} and $n = 0.5$. The scale bar is 1 nm in all images.

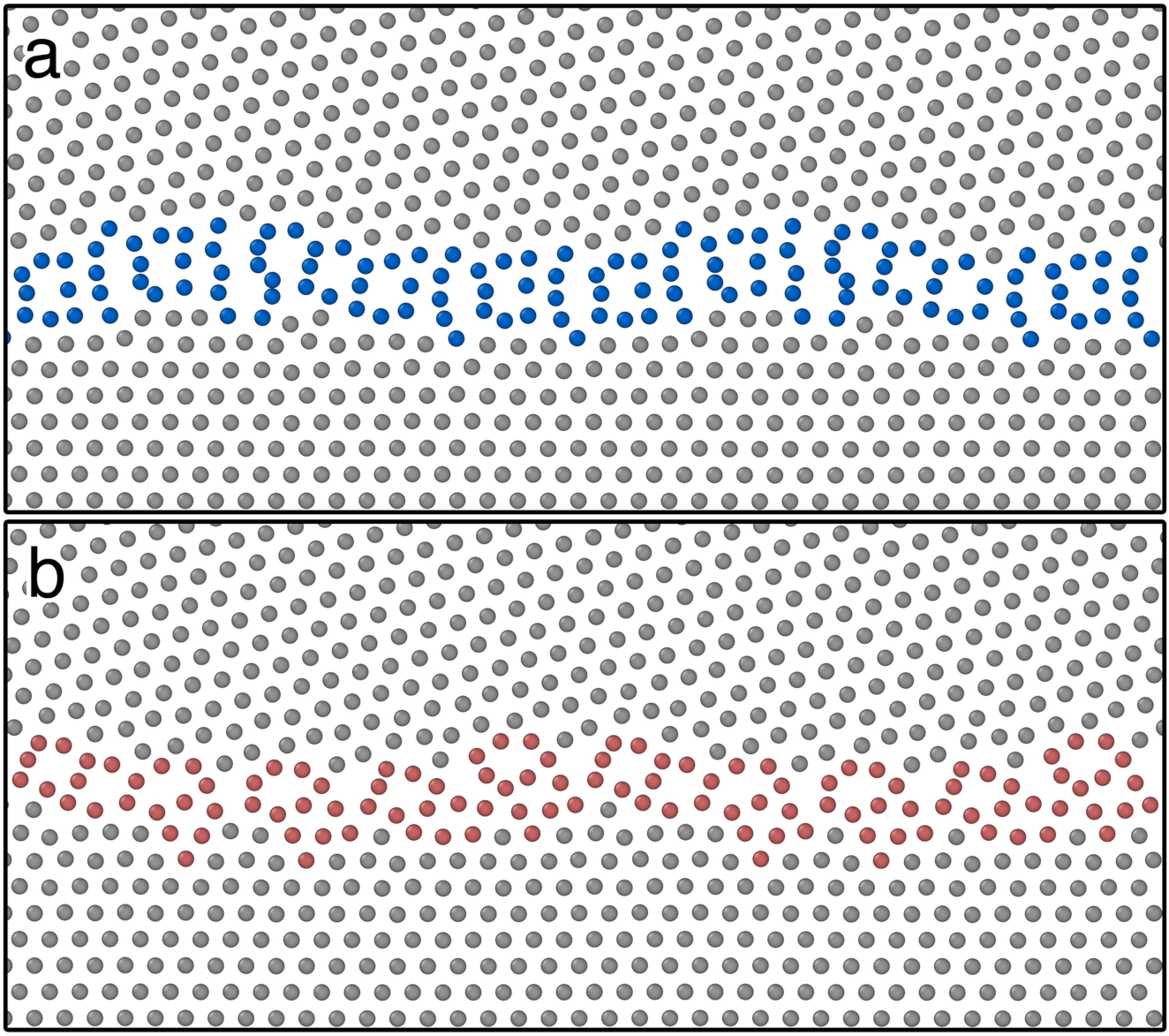

Extended Data Fig. 4 | Asymmetric GB structures. a, **b**, Ground-state pearl (**a**) and metastable domino (**b**) structures of the asymmetric boundary at 0 K. The two structures have the same number of atoms and correspond to two different translations of the bulk grains relative to each other.

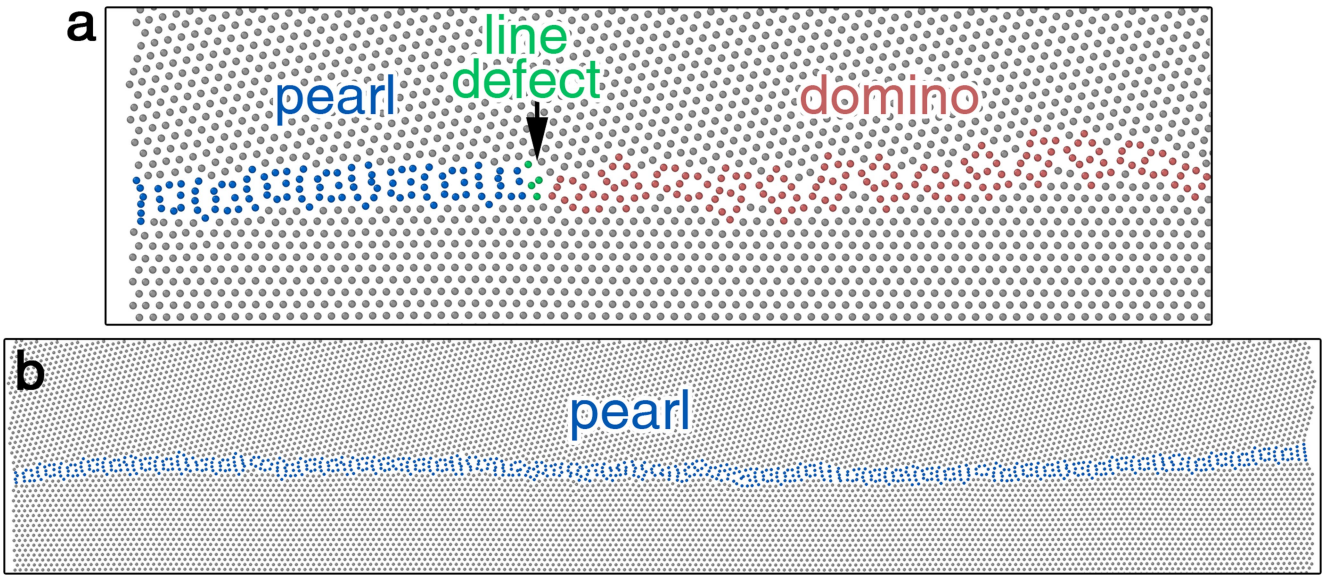

Extended Data Fig. 5 | Asymmetric GB transformation at 600 K. a, Nucleation of a pearl GB phase at the open surface (left) of the asymmetric GB at 600 K. **b**, Asymmetric pearl GB phase after the transformation at 600 K is complete. The boundary remains asymmetric.

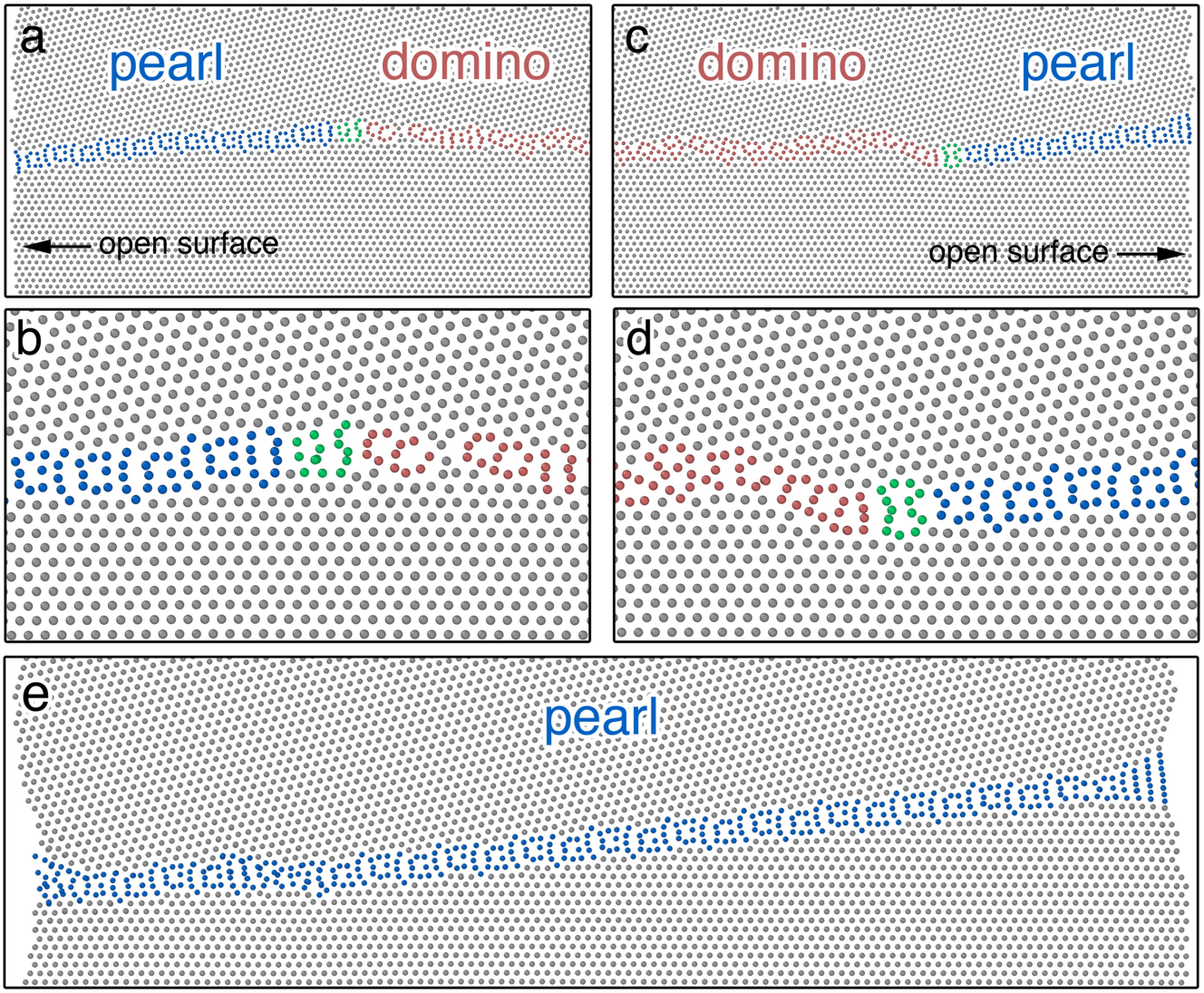

Extended Data Fig. 6 | Asymmetric GB transformation at 700 K. a and **b** show the nucleation of the pearl GB phase from the open surface on the left of the simulation cell annealed at 700 K. **c** and **d** from the right. **e**, The initially asymmetric domino structure transformed into a symmetric pearl phase in MD at 700 K after the transformation is complete.

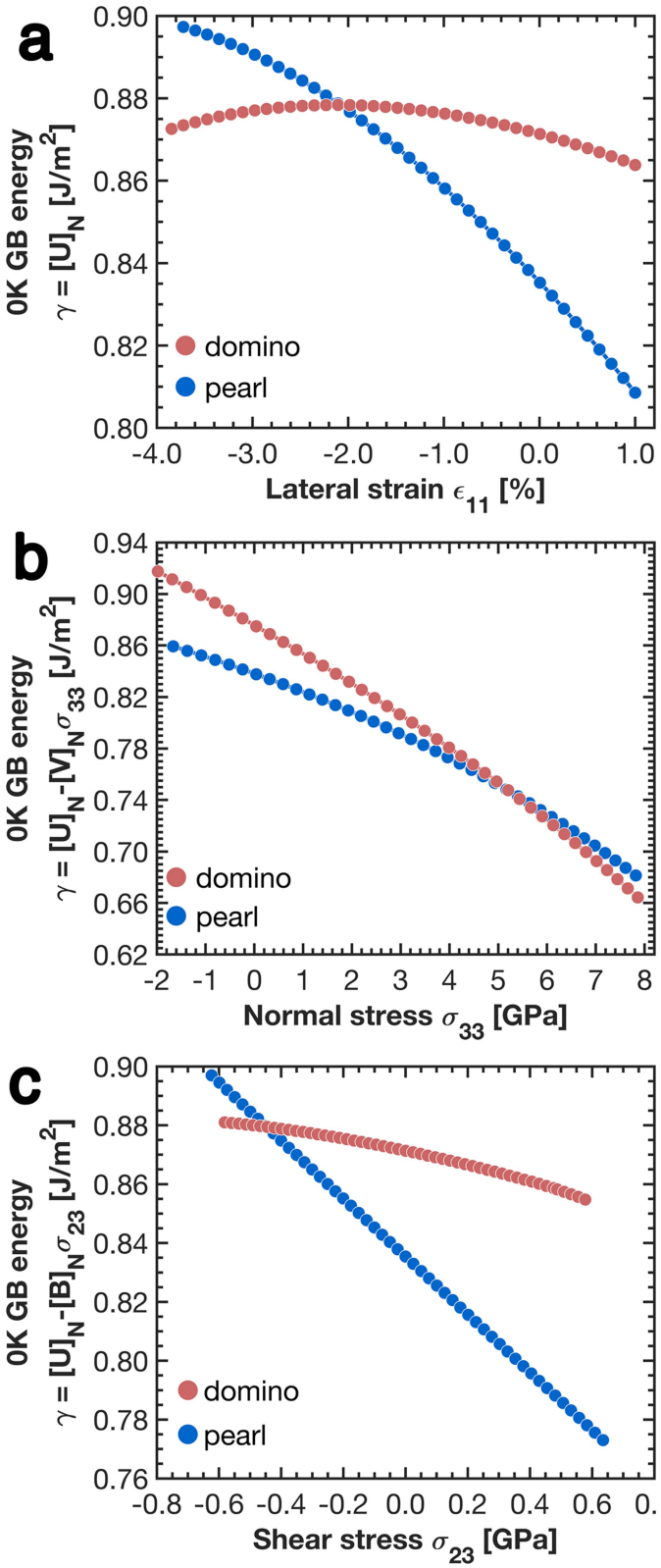

Extended Data Fig. 7 | Stress-dependent GB excess enthalpies. 0 K calculations of GB excess enthalpies γ_{domino} and γ_{pearl} to estimate stresses and strains required to stabilize the domino phase and achieve equilibrium coexistence in the model. GB excess energy curves cross at: **a**, lateral strain $\varepsilon^*_{11} = 2\%$; **b**, tensile stress $\sigma^*_{33} = 5$ GPa; and **c**, shear stress parallel to the GB along the tilt axis $\sigma^*_{23} = 440$ MPa. $[U]_N$, $[V]_N$ and $[B]_N$ are the excess GB energy, volume and shear, respectively.

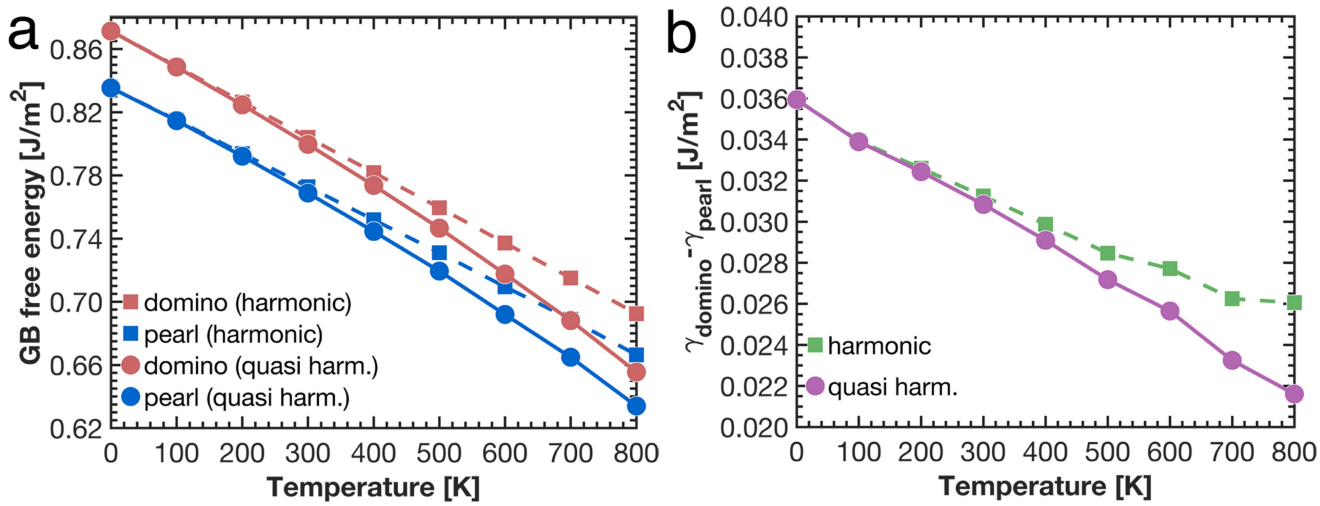

Extended Data Fig. 8 | GB free energies. a, GB free energies of domino and pearl phases as functions of temperature at zero bulk stress calculated using harmonic and quasi-harmonic approximations. **b**, The GB free energy difference $\gamma_{domino} - \gamma_{pearl}$ as a function of temperature decreases but remains positive suggesting that at ambient pressure the domino phase remains metastable in our model. These calculations are consistent with domino to pearl transformations simulated directly with MD. They also show that in the model the relative stability of the domino phase improves with temperature since the GB free energy difference decreases by about 30% relative to 0 K.

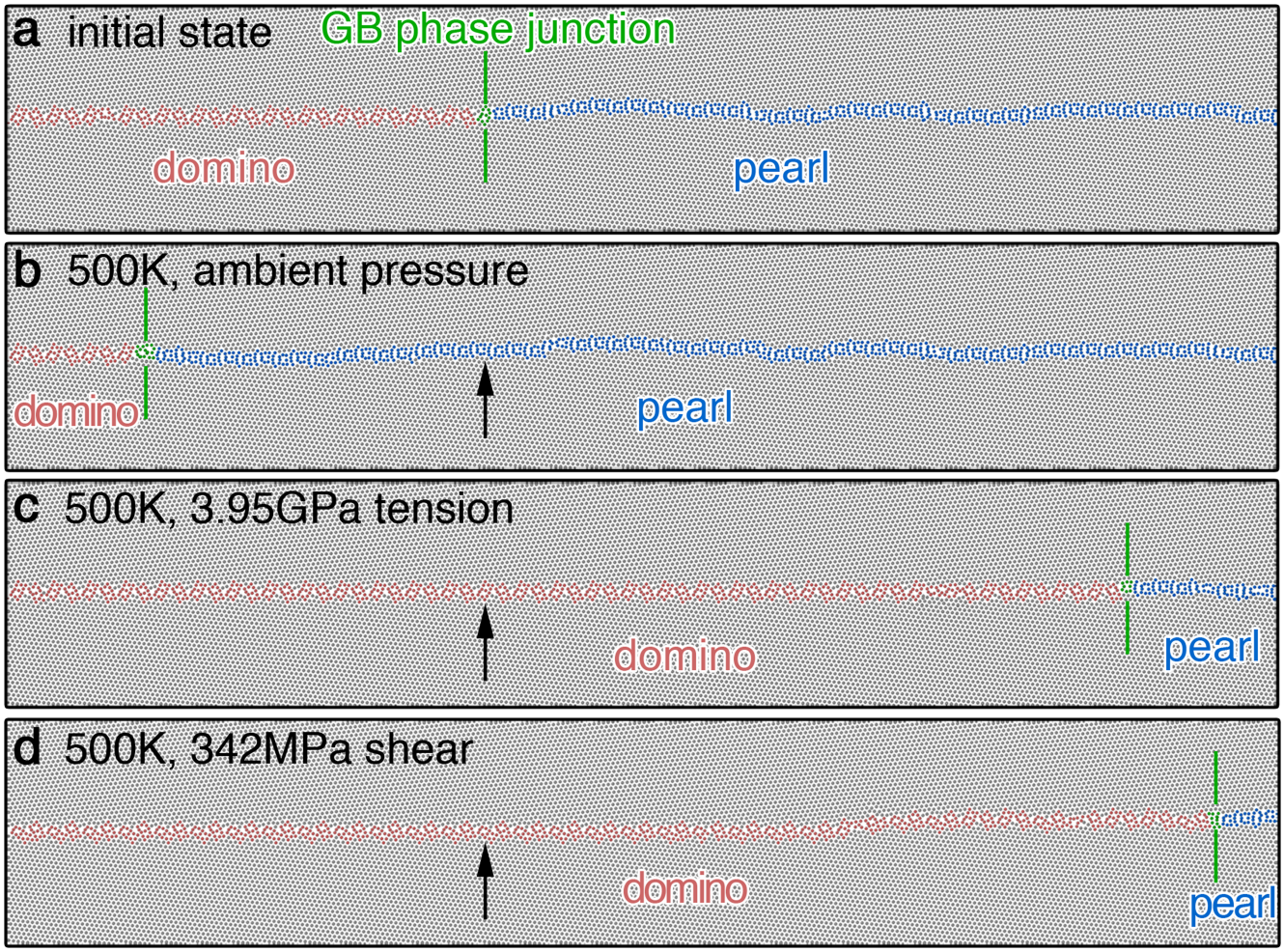

Extended Data Fig. 9 | Finite temperature GB phase transformations under stress. MD simulations of GB phase transformations and equilibrium coexistence at 500 K under ambient conditions (**a**, **b**), tensile stress (**c**) and shear stress (**d**). **a**, To avoid hysteresis due to the nucleation barrier we start with a two-phase state (**a**) and monitor the direction of the GB phase junction migration. **b**, At ambient conditions the pearl phase grows and the junction moves to the left. **c**, Under tensile stress of 3.95 GPa the domino phase becomes thermodynamically more stable, it grows at the expense of the pearl phase and the junction moves to the right. **d**, Under a shear stress of 342 MPa parallel to the GB plane in the direction parallel to the tilt axis the domino phase also becomes more stable and grows. The black arrow indicates the initial position of the GB phase junction, while the green line shows the final position. We performed similar simulations at different tensile and shear stresses and conclude that in the model the equilibrium coexistence between the pearl and domino phases at this temperature of 500 K can be achieved at around 3.3 GPa tension or within the range 200–350 MPa for shear stress. The simulations of equilibrium coexistence confirm that pearl and domino are examples of GB phases. The MD simulations ran for 200 ns to 400 ns.

Extended Data Table 1 | Excess thermodynamic properties.

GB phase	Energy [J/m^2]	Volume [Å]	Stress τ_{11} [J/m^2]	Stress τ_{22} [J/m^2]	[n]
Pearl	0.835	0.14	-1.66	-0.46	0
Domino	0.871	0.22	0.25	0.29	0

The table shows the energy, excess volume, excess stress and number of inserted atoms *n* of the ground-state pearl and the lowest-energy domino GB phases determined at 0 K.